Journal of Materials Chemistry A

ROYAL SOCIETY OF CHEMISTRY

PAPER

View Article Online
View Journal | View Issue

Cite this: J. Mater. Chem. A, 2023, 11, 19384

Enabling uniform zinc deposition by zwitterion additives in aqueous zinc metal anodes†

Sung-Ho Huh,‡[a] Yoon Jeong Choi,‡[a] So Hee Kim,[b] Jong-Seong Bae,[c] Si-Hwan Lee[a] and Seung-Ho Yu *[a]

Received 31st March 2023
Accepted 15th August 2023

DOI: 10.1039/d3ta01943h

rsc.li/materials-a

The rechargeable aqueous zinc metal battery is considered one of the most promising next-generation batteries for energy storage systems, owing to its low negative standard reduction potential (−0.76 *vs.* the standard hydrogen electrode (SHE)), low cost of zinc and water, and no fire-risk. However, the formation of zinc dendrites and hydrogen evolution hinder the commercialization of rechargeable aqueous zinc metal batteries. In this study, we investigate the use of 6-aminohexanoic acid (6-AA), a type of amino acid, as an electrolyte in a 1 M $ZnSO_4$ solution. The 6-AA molecules become zwitterions, reducing side reactions by adsorbing onto the zinc metal surface and blocking water molecules and other ions, except for zinc ions. Additionally, the adsorbed 6-AA molecules hinder the two-dimensional diffusion of zinc ions on the zinc metal surface and thereby reduce the formation of zinc dendrites. The 6-AA additive enables reduced corrosion, and uniform zinc deposition is observed. Moreover, both the Zn||Zn symmetric cell and Zn||Cu cell with the 6-AA added electrolyte exhibit a long cycle life, and the α-MnO_2||Zn full cell shows improved cycle performance by using the 6-AA additive.

Seung-Ho Yu is an associate professor of the Department of Chemical and Biological Engineering at Korea University, which he joined in 2019. He received BS (2008) and PhD (2013) from the School of Chemical and Biological Engineering at Seoul National University. He worked as a researcher at the Research Institute of Advanced Materials (RIAM) and as a senior researcher at the Center for Nanoparticle Research in the Institute for Basic Science (IBS) at Seoul National University. From 2015 to 2019, he was a post-doctoral associate in the Department of Chemistry and Chemical Biology at Cornell University. His current research focuses on designing electrode materials and revealing reaction mechanisms of electrode materials for Li-ion and post-Li-ion batteries.

Introduction

Decarbonization is considered a significant policy to mitigate recent climate change and global warming. To achieve this goal, various efforts are focused on electricity production through renewable energy sources such as solar panels and wind power plants.[1] Unlike conventional fossil fuel power plants, however, renewable energy sources such as sunlight and wind cannot provide a steady supply of energy due to environmental and temporal factors. Due to this reason, the need for an energy storage system that can store the produced energy and supply it consistently later has arisen.[2] Currently, lithium-ion batteries, which are widely used in electric cars and portable electronic devices, are difficult to use in large-scale energy storage systems due to the high cost of lithium and cathode material, and the risk of fire with organic solvent-based electrolytes.[3,4] To solve these problems, a water-based battery system that uses low-cost and safe electrolytes is needed.

As a result, the rechargeable aqueous zinc metal battery is receiving attention as a safe and high-capacity next-generation battery due to the high theoretical capacity of zinc metal as a negative electrode (820 mA h g^{-1}), low standard reduction potential (−0.76 V *vs.* the standard hydrogen electrode (SHE)),

[a]Department of Chemical and Biological Engineering, Korea University, 145 Anam-ro, Seongbuk-gu, Seoul 02841, Republic of Korea. E-mail: seunghoyu@korea.ac.kr

[b]Advanced Analysis Center, Korea Institute of Science and Technology (KIST), Seoul 02792, Republic of Korea

[c]Busan Center, Korea Basic Science Institute (KBSI), 30 Gwahaksandan 1-ro, 60 Beon-gil, Gangseo-gu, Busan 46742, Republic of Korea

† Electronic supplementary information (ESI) available. See DOI: https://doi.org/10.1039/d3ta01943h

‡ These authors contributed equally to this work.

low cost, and the use of an aqueous electrolyte system with lower fire risk and cost compared to organic materials.[5,6] However, during the deposition/stripping process of zinc metal, the growth of zinc dendrites occurs, leading to the formation of dead zinc during the stripping process, which causes low Coulombic efficiency or internal short-circuiting due to continuous dendritic growth and self-discharge.[7] Additionally, the zinc metal surface in contact with the aqueous electrolyte is corroded, forming an insulating film such as oxide, which hinders capacity performance in that area.[8] Furthermore, since the oxidation–reduction potential of zinc is lower than the hydrogen evolution potential of water, hydrogen gas is generated during the zinc deposition process.[7,8] This can cause volume expansion of the battery and, in extreme cases, even explosion. At the same time, the concentration of hydroxide ions (OH^-) increases around the electrode, reacting with zinc metal and other anions to form zinc basic sulfate (ZBS) on the electrode surface, which causes low Coulombic efficiency.[9]

Various approaches are being studied to address the problems of zinc-based batteries. Representative research approaches include (1) coating layers, (2) zinc alloy electrodes, and (3) electrolyte additives. The coating technique suppresses the physical growth of zinc on the surface of the zinc metal by applying an ion-conductive coating layer, which prevents direct contact between the electrolyte and the zinc electrode, thus inhibiting the corrosion of the electrode and hydrogen evolution.[10–12] Coating options include porous structures such as ZIF-11[10] and ZIF-8,[11] and polymers such as polyamide.[12] Additionally, research exists on using dielectric coatings to control the diffusion of specific ions by changing the charge direction of the dielectric depending on the current direction. However, coating layers are vulnerable to external impacts and can cause zinc to grow on exposed areas when damaged. Also, when the coating layer is formed unevenly, there is a problem of uneven zinc ion (Zn^{2+}) diffusion, which hinders the suppression of dendritic zinc growth.[13] In the case of alloy electrodes such as Zn–Cu,[14] Zn–Sn,[15] and Zn–Al,[16] using metals that create a uniform alloy with zinc to make alloy electrodes reduces the binding energy of the electrode surface, promoting uniform zinc deposition or forming an alloy between the electrode and zinc to suppress growth on the surface. However, the problem is in the difficulty of forming the alloy electrode or using heavy metals.[17] Electrolyte additives, used by dissolving specific metal cations[18] or organics,[19] modify the solvation structure of Zn^{2+} or prevent water molecules from approaching the electrode by adsorbing on the zinc metal surface, or suppress concentrated zinc deposition through shielding effects.[18] Recently, research has been reported on the *in situ* formation of a uniform coating layer on the electrode surface by electrolyte additives during the charging and discharging process.[20]

Zwitterions such as amino acids and betaine exhibit characteristics of both anions and cations when utilized as a water-based electrolyte additive, as they possess both cationic and anionic functional groups. The anionic groups can form a solvation structure with Zn^{2+} and lower the reactivity of water molecules.[21–23] The cation groups adsorb near the zinc metal surface and regulate the Zn^{2+} adsorption.[21,22] Moreover, the anion tail of zwitterions can repel the water molecules and other anions, such as SO_4^{2-} from the zinc metal surface and reduce ZBS formation.[22,23]

Herein, due to the unique ability of zwitterions, we use 6-aminohexanoic acid (abbreviated as 6-AA) as an electrolyte additive. The 6-AA added electrolyte shows a higher pH value with lower zinc metal corrosion and hydrogen evolution. Additionally, the 6-AA additive reduces zinc dendrite growth and 2D diffusion of Zn^{2+}, and enables uniform zinc deposition which is visualized by the top-view *operando* optical technique. In addition, we have discovered that the 6-AA additive promotes zinc deposition in a specific crystal orientation. With these properties, the electrolyte additive showed an improved cycle life by about four times in symmetric cell tests and demonstrated an enhanced lifespan in Zn‖Cu cells. Furthermore, stable cycling was observed even at a high current density of 4 mA cm^{-2}. Moreover, an cycle performance was improved in full cells using α-MnO_2 with the 6-AA additive.

Experimental

Materials preparation

To make a blank electrolyte, 0.1 mol of $ZnSO_4 \cdot 7H_2O$ was dissolved in deionized water until it reached 100 mL. The electrolytes with 6-AA were prepared by adding 0.3, 0.5, and 0.7 M 6-AA to 50 mL of blank electrolyte. The optimized concentration of 6-AA is 0.5 M, and it is denoted as 6-AA added electrolyte in this work.

Manganese dioxide (α-MnO_2) is synthesized for the full cell test. 0.9482 g of potassium manganate(VII) ($KMnO_4$) and the 2.206 g of manganese(II) acetate tetrahydrate ($Mn(CH_3COO)_2 \cdot 4H_2O$) were mixed with a grinding bowl. The obtained powder was transferred to an alumina boat and thermally treated at 120 °C for 4 hours in a furnace with a heating rate of 5 °C min^{-1}. After cooling to room temperature, the product was ground and washed three times with deionized water and then dried in an oven at 80 °C for overnight. The α-MnO_2 cathode electrode for the full cell test was fabricated by mixing α-MnO_2 as the active material, Super P as the conductive agent, and polyvinylidene fluoride (PVDF) as the binder in a weight ratio of 8 : 1 : 1. After mixing in an agate mortar, the slurry was dried in a vacuum oven at 80 °C for 12 h. The mass loading of α-MnO_2 is 1.9–2.2 mg cm^{-2}. For the Zn symmetrical pouch cell, 5 cm × 5 cm of Zn foil is used as both working electrode and counter electrodes, and the total volume of electrolyte was 5 mL.

Characterization

The fundamental structures of the electrolytes were analysed by using a Fourier-transform infrared spectrometer (FT-IR; Thermo Fisher Scientific Nicolet IS50) and Raman spectroscope (Thermo Fisher DXR3xi). The Raman spectra were acquired using lasers with a wavelength of 532 nm as shown in Fig. 1c–e. The pouch cell weight in water was measured by the Archimedes method used in previous work.[24] The measurements of the contact angle with various electrolytes were obtained by using a contact angle meter (Kruss DSA 25). The

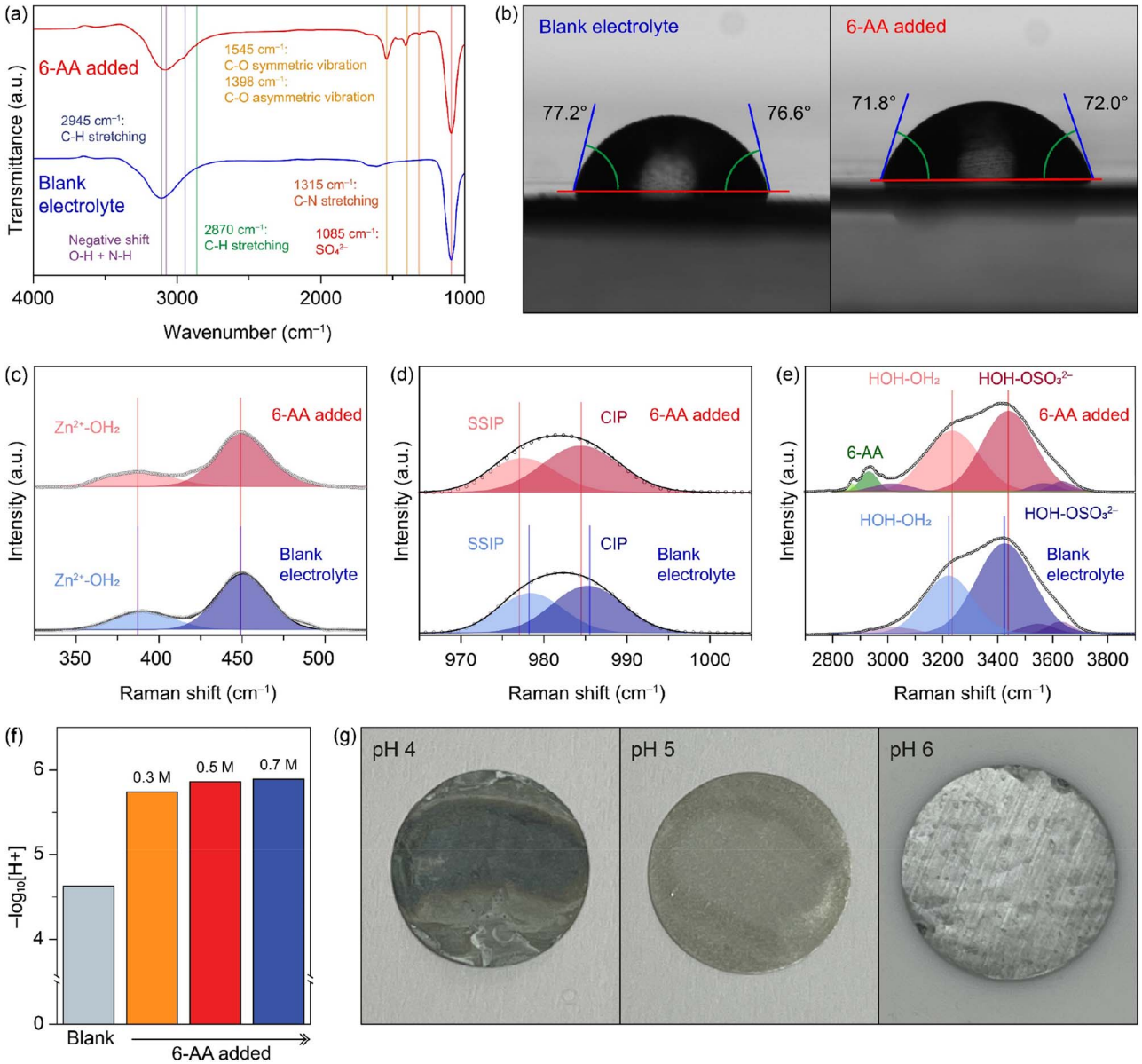

Fig. 1 (a) FTIR spectra of the blank electrolyte (blue) and the 6-AA added electrolyte (red). (b) The optical images of the contact angle between the zinc foil and the electrolyte ((left) the blank electrolyte and (right) the 6-AA added electrolyte). Raman spectra with the Raman shift range of (c) 325–525 cm^{-1}, (d) 965–1005 cm^{-1}, and (e) 2700–3900 cm^{-1} (blue: the blank electrolyte and red: the 6-AA added electrolyte). (f) pH values of the blank electrolyte and the various concentrations of the 6-AA added electrolyte. (g) Optical images of zinc foil immersed in buffer solution of pH 4, 5, and 6 for 5 days.

crystal structures of all zinc electrodes were determined by X-ray diffraction (XRD; Rigaku SmartLab) with Cu with Cu Kα radiation ($\lambda = 1.5406$ Å) over a 2θ range of 10–80° with a step size of 0.02°. X-ray photoelectron spectroscopy (XPS) spectra were obtained from a Sigma Probe (Thermo Fisher Scientific, UK). Monochromated Al Kα (1486.6 eV) was used as the X-ray source. CasaXPS software was used to fit the XPS spectra. The top-view and side-view scanning images and corresponding EDS elemental maps were obtained using field emission scanning electron microscopy (FE-SEM; Hitachi, Regulus 8230) performed at 15 kV. The X-ray fluorescence images (XRF) were recorded at the Pohang Accelerator Laboratory (PAL) on beamline 4B. *Operando* microscopy analysis in Fig. 4 was performed using a coin cell with a 5 mm diameter hole by using optical microscopy (OM; ×50 lens, ECLIPSE LV150N, Nikon), the same method used in previous work.[25] The pH test was carried out by using a pH meter (OHAUS ST350).

Electrochemical test

CR2032 coin cells were used to perform all the electrochemical tests in this work, and all the electrochemical tests were conducted on a WonATech cycler at 25 °C. The separator for coin cells was fixed with porous glass fiber (Whatman, GF/C). The electrolyte volume for all the batteries was 100 μL. For the

Zn||Zn symmetric cells, two 16 mm zinc foils were punched into discs and were filled with a blank electrolyte or 6-AA added electrolyte. The Zn||Cu half-cell was assembled with copper foil as a cathode and zinc foil as an anode. The α-MnO_2||Zn full cells were assembled using 16 mm zinc foil and 11 mm α-MnO_2 electrodes with the blank electrolyte or the 6-AA added electrolyte. The three-electrode coin cells for the Tafel plot and linear sweep voltammetry (LSV) were assembled in the same way as previous research.[26] For the Tafel plot, a 16 mm zinc disk was used as the working electrode and the counter electrode. Also, carbon paper was used as the counter electrode and the working electrode for LSV hydrogen evolution analysis. For the three-electrode assembly, the zinc reference electrode which stretched out the cell was sandwiched between the working electrode and counter electrode with two porous separators.

Cycling voltammetry was performed by scanning between −0.2 and 0.5 V at 0.1 mV s^{-1} with a Zn||Cu cell. Electrochemical impedance spectroscopy (EIS) of the Zn||Zn symmetric cell was performed at an amplitude of 10 mV within a range from 1 MHz to 0.1 Hz. The Zn^{2+} transference number was estimated by EIS before and after the chronoamperometry (CA) test at an overpotential of 50 mV and calculated by using the following equation.[27]

$$t_+ = \frac{(\Delta V/I_O - R_0)}{(\Delta V/I_{SS} - R_{SS})}$$

Chronoamperometry was conducted with the zinc symmetric cell at 150 mV overpotential for 1200 s. The initial zinc deposition overpotential graphs of the blank electrolyte and the 0.5 M 6-AA added electrolyte were estimated with the zinc symmetric cell at 5 mA cm^{-2}. The cyclability of the Zn symmetric cell was tested at 1 mA cm^{-2} and 1 mA h cm^{-2}, and the rate capability of the Zn symmetric cell was determined with a fixed areal capacity of 1 mA h cm^{-2} at 1, 2, 5, and 10 mA cm^{-2} for 10 cycles with the subsequent cycle conditions of 1 mA cm^{-2} and 1 mA h cm^{-2}. The Zn||Cu half-cell was tested at 4 mA cm^{-2} and 2 mA h cm^{-2}.

Full cells were assembled using α-MnO_2 as the cathode, Zn foil as the anode, 1 M $ZnSO_4$ + 0.2 M $MnSO_4$ as the blank electrolyte for the full-cell, and 1 M $ZnSO_4$ + 0.2 M $MnSO_4$ + 0.5 M 6-AA as 6-AA added electrolyte for the full-cell. α-MnO_2||Zn full cell charge/discharge tests were conducted at 0.2 A g^{-1} and 0.5 A g^{-1} with a cut-off voltage from 0.9 V to 1.8 V *vs.* Zn^{2+}/Zn. The cyclic voltammetry test of the α-MnO_2||Zn full cell was conducted by scanning between 0.9 V and 1.8 V at a scan rate of 0.2 mV s^{-1}.

Results and discussion

6-Aminohexanoic acid added electrolyte (abbreviated as 6-AA added electrolyte) was synthesized by simply adding 0.5 M 6-AA to blank electrolyte (1 M $ZnSO_4$). Fig. 1a shows the Fourier-transform infrared spectroscopy (FTIR) spectra of the blank electrolyte (blue line) and the 6-AA added electrolyte (red line). Both spectra show a characteristic peak at 1085 cm^{-1} and a broad peak at 3200–3100 cm^{-1}. The strong peak at 1085 cm^{-1} indicates the presence of SO_4^{2-}, which comes from $ZnSO_4$, and the broad peak at 3200–3100 cm^{-1} indicates O–H, which originates from the H_2O molecules.[28] The red shift of the broad peak in the 6-AA added electrolyte spectrum indicates the hydrogen attraction ability and the N–H bond in 6-AA.[29–31] Moreover, the 6-AA added electrolyte shows additional peaks at 2945, 2870, 1545, 1398, and 1315 cm^{-1}, which are related to C–H stretching, C–O vibration and C–N stretching.[32,33] The absence of the C=O bond in the carboxylic acid group (–COOH) peak indicates the ionization of carboxylic acid to carboxylate of 6-AA in water. Fig. S1† displays the difference FTIR spectra of 6-AA under different pH conditions. The C=O bond peak is only identified under pH 1 conditions, not under pH 7 and pH 14 conditions, which is consistent with the pK_a value of 6-AA.[34]

The wettability test was conducted to verify the affinity of the electrolyte with zinc metal (Fig. 1b and S2†). The initial contact angle on the zinc surface is smaller with the 6-AA added electrolyte than with the blank electrolyte (99.9° *vs.* 92.5°) (Fig. S2†). Additionally, after 5 minutes, the average contact angle for the blank electrolyte is 76.9°, and for the 6-AA added electrolyte it is 71.9°. The smaller contact angle of the 6-AA added electrolyte results from the fact that 6-AA molecules disrupt the hydrogen bonding network of water molecules and lowers the surface tension.[35] Additionally, the 6-AA molecules act as chelating agents and adsorb on the zinc metal surface, which can increase the zinc metal affinity of the electrolyte.[36,37] The wettability test results on copper foil also show a similar contact angle regardless of the presence of the 6-AA additive, which confirms that the 6-AA additive does not change the copper affinity of the electrolyte (Fig. S3†). The higher affinity of the electrolyte to metal foil decreases the interfacial energy between the electrolyte and metal foil, thereby enabling uniform zinc nucleation and uniform zinc deposition.[38,39] The adsorption of 6-AA molecules on the metal surface was further estimated by X-ray photoelectron spectroscopy (XPS) (Fig. S4†). The R-NH_2 peak in the N 1s spectrum was observed for zinc and copper foil that had been immersed in the 6-AA added electrolyte for 6 hours. This indicates that 6-AA molecules were adsorbed on the Zn surface. The FT-IR spectra of 6-AA powder and Zn metal after immerging in the electrolyte with 6-AA (Fig. S5†) also support the adsorption of 6-AA on the Zn metal. Raman spectra in Fig. 1c–e show the bond between ions and water molecules and the solvation structure of ions in the blank electrolyte (blue line) and the 6-AA added electrolyte (red line). The spectra in Fig. 1c–e indicate Zn^{2+}–OH_2 interaction, the solvation structure of $ZnSO_4$, the interaction of H_2O and SO_4^{2-}, each.[40,41] The Zn^{2+}–OH_2 bond peaks at 387 cm^{-1} in the blank electrolyte spectrum and the 6-AA added electrolyte spectrum show the same Raman shift, which indicates that the binding energy between Zn^{2+} and water molecules is not interrupted by the 6-AA molecules. However, in Fig. 1d, the red shift of SSIP and CIP peaks in the 6-AA added electrolyte is shown. The red shift of the Raman peak results from the relatively free molecular motion, which indicates a loose solvation structure in the 6-AA added electrolyte.[42] Also, in Fig. 1e, the hydrogen bond peak and H_2O–SO_4^{2-} interaction also show a blue shift in the spectrum of the 6-AA added electrolyte, which also shows strong interaction among

water molecules and other ions by the 6-AA additive.[42] This can be interpreted as due to the introduction of 6-AA molecules which suppress the H_2O induced side reactions because of the weak solvation structure and relatively intensive interaction between water molecules. The reduced side reactions of water molecules are further investigated as below.

The 6-AA dissociation analysis was conducted through a simple pH measurement. The pH values for electrolytes with different concentrations of 6-AA are shown in Fig. 1f. It was observed that at 6-AA concentrations of 0.3, 0.5 and 0.7 M, the pH values increased to 5.74, 5.86 and 5.89, respectively, compared to the blank electrolyte which had a pH value of 4.63. As the pK_a value of 6-AA is known to be 4.43 for the carbonyl group and 10.75 for the amine group, the pI value is 7.59 which can be expected because 6-AA molecules exist as a zwitterion near this pH condition.[34] Moreover, as shown in Fig. 1g, the corrosion test of zinc metal under various pH conditions was conducted. The optical image shows that the zinc surface blackens by corrosion at pH 4, relatively whitens at pH 5, and maintains its original silver-grey surface at pH 6. According to the corrosion test and the pH measurement, the corrosion of zinc metal in the 6-AA added electrolyte is inhibited due to the higher pH value compared to the corrosion and side reaction in the blank electrolyte, which is discussed in later sections. The linear polarization test was conducted to investigate the corrosion of the zinc electrode with a three-electrode zinc symmetric cell. Fig. 2a shows the Tafel curve of the blank electrolyte (black line) and 6-AA added electrolyte (red line). The corrosion voltage in the 6-AA added electrolyte (0.0232 V *vs.* Zn^{2+}/Zn) is higher than that in the blank electrolyte (0.0178 V *vs.* Zn^{2+}/Zn). In addition, the corrosion current density is also lower in the 6-AA added electrolyte (0.00915 mA cm^{-2}) than in the blank electrolyte (0.03055 mA cm^{-2}). This indicates that the 6-AA additive inhibits the corrosion of the zinc metal surface.[43,44] An additional linear polarization test was also conducted to test the hydrogen evolution reaction of the electrolytes in a three-electrode cell with carbon paper as a working and a counter electrode (Fig. 2b). The linear sweep voltammetry (LSV) curves show a steeper slope at a higher voltage in the blank electrolyte compared to the case in the 6-AA added electrolyte, indicating that the 6-AA additive suppresses the hydrogen evolution. Also, the hydrogen evolution is further investigated by measuring the changes of coin cell heights and pouch cell weights in water using Archimedes methods (Fig. S6 and S7†). It was observed that the volume expansion of the cell was significantly higher under the blank electrolyte conditions that the volume expansion in Zn||Zn cells during the cycling process at 1 mA cm^{-2} and 1 mA h cm^{-2}. This was confirmed by the side-view image of the coin cell after the 150th cycle, which showed greater volume expansion in the blank electrolyte compared to the 0.5 M 6-AA added electrolyte (Fig. S6†). The more rapid decrease of the pouch cell weight in the blank electrolyte than that with the 6-AA electrolyte supports the suppressed hydrogen evolution in the cell with 6-AA at a given amount of time (Fig. S7†). Besides, the cyclic voltammogram (CV) curves in Fig. 2c show no additional peaks in the 6-AA added electrolyte compared to the curve of the blank electrolyte, showing that additional reactions do not occur, although the cathodic peak potential is higher in the 6-AA added electrolyte, indicating a higher zinc stripping overpotential.

To verify the corrosion of zinc metal in each electrolyte, the zinc metal was immersed in each electrolyte for 7 days. Fig. 2d displays the optical image of the immersed zinc foil, the blank electrolyte in the top-left corner and the 6-AA added electrolyte in the bottom-right corner. The optical image clearly shows that the zinc foil immersed in the blank electrolyte is severely corroded, but the zinc foil immersed in the 6-AA added electrolyte retains its silver-grey surface. The scanning electron microscope (SEM) image and energy dispersive X-ray spectroscopy (EDS) mapping data also ensure that the corrosion of zinc metal is suppressed by the 6-AA additive (Fig. 2e and S8†). The SEM and EDS data of the zinc foil immersed in the blank electrolyte show that the zinc metal surface is completely covered with hexagonal flakes, consisting of zinc, oxygen, and sulfur. In contrast, smaller hexagonal flakes and fresh zinc metal surface are observed in the zinc foil immersed in the 6-AA added electrolyte. This confirms the corrosion suppression ability of 6-AA molecules. X-ray diffraction (XRD) was performed for further investigation of corrosion of zinc metal in the electrolyte (Fig. 2f). As the difference between the XRD patterns (black: blank electrolyte and red: 6-AA added electrolyte) are not clear, the magnified XRD patterns are shown in Fig. 2f(i) and (ii), which correspond to the 24–36° region and 49–61° region, respectively. Fig. 2f(i) shows that side reaction byproduct peaks are found in zinc metal immersed in the blank electrolyte, which are consistent with $Zn_4(OH)_6(SO_4)\cdot 4H_2O$ (zinc basic sulfate, ZBS) peaks.[45] In comparison, in the 6-AA added electrolyte, a significantly smaller number of peaks are visible with lower intensity. Similarly, in the XRD pattern of the zinc metal immersed in the 6-AA added electrolyte, no ZBS peaks and ZnO peak are observed, confirming that the 6-AA additive suppresses the corrosion of zinc metal in the aqueous electrolyte.[45,46] The effect of the 6-AA additive on the deposition of zinc metal was measured by electrochemical and morphological experiments. The chronoamperometry (CA) results in Fig. 3a demonstrate fast stabilization of 2D diffusion in the 6-AA added electrolyte ($\leq$30 s), whereas longer 2D diffusion occurs in the blank electrolyte ($\geq$200 s). The initial region with a steep slope of the current density represents the 2D diffusion of Zn^{2+} near the electrode, while the stable and flat current density region represents the 3D diffusion of Zn^{2+}.[47] The faster current stabilization shows that the 6-AA molecules on the zinc metal surface act as an additional resistance, preventing the diffusion of Zn^{2+} on the metal surface. This phenomenon helps to form a uniform nucleation site, in contrast to the blank electrolyte where deposition occurs at a uneven nucleation site.[48,49] The deposition overpotential test at 5 mA cm^{-2} also provides the evidence that more uniform zinc deposition occurs in the 6-AA added electrolyte (Fig. 3b and S9†). Previous research has shown that there is a correlation between a higher nucleation overpotential and the formation of smaller-sized, higher density nuclei.[50] In addition, higher growth overpotential can be attributed not only to the increased resistance of zinc deposition but to the relatively smaller surface area due to the uniform

deposition of zinc metal, indicating that zinc growth in the blank electrolyte causes more dendritic growth compared to the case of the 6-AA added electrolyte.[51] Electrochemical impedance spectroscopy (EIS) was conducted to determine the charge transfer resistance from the electrolyte to the zinc metal surface in each electrolyte (Fig. 3c). The Nyquist plots show that the charge transfer resistance in the 6-AA added electrolyte is lower than in the blank electrolyte. The higher Zn^{2+} transfer resistance in the blank electrolyte may result from the passivation layer formation (ZBS or ZnO) by a side reaction and hydrogen evolution on the metal surface.[17] Besides, the adsorption of 6-AA molecules on the zinc metal surface forms a protection layer which decreases the side reaction and hydrogen evolution by blocking the direct contact between the zinc metal and electrolyte. Additionally, the Zn^{2+} transference number ($t_{Zn^{2+}}$) calculation with a symmetric cell in EIS and CA data demonstrate that the blank electrolyte and the 6-AA added electrolyte have similar $t_{Zn^{2+}}$ (0.238 *vs.* 0.234) (Fig. S10†). This indicates

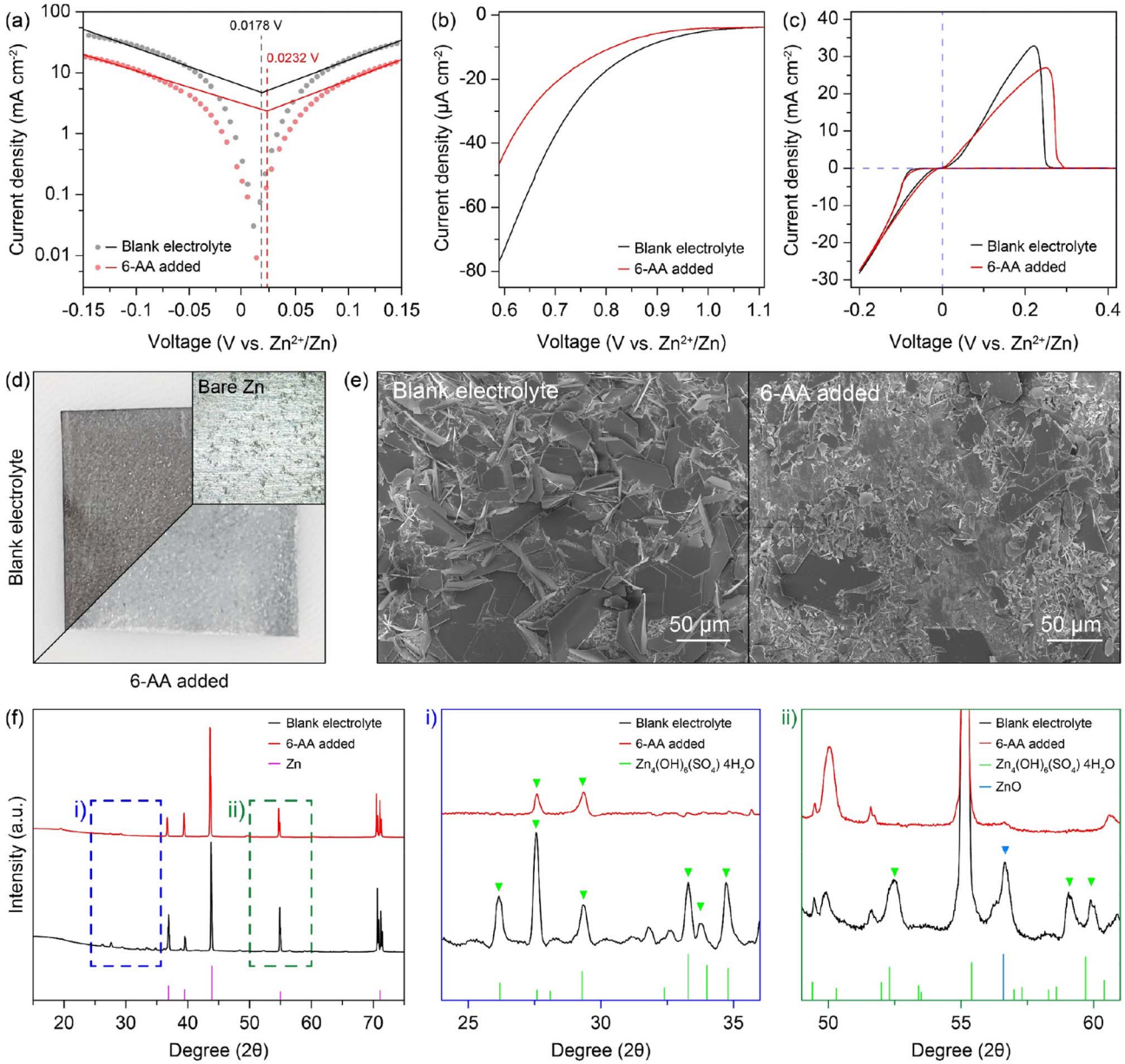

Fig. 2 (a) Tafel plots of the three-electrode zinc symmetric cell, representing a lower corrosion exchange current and higher corrosion voltage in the 6-AA added electrolyte than the blank electrolyte. (b) Linear sweep voltammetry (LSV) curves of the three-electrode carbon paper symmetric cell, indicating less hydrogen evolution in the 6-AA added electrolyte. (c) Cyclic voltammogram (CV) curves of the Zn||Cu cell. (d) Optical images of bare zinc foil and zinc foils immersed in the blank electrolyte and the 6-AA added electrolyte. (e) Top-view scanning electron microscopy (SEM) images of zinc foils immersed in the blank electrolyte and the 6-AA added electrolyte. (f) X-ray diffraction (XRD) patterns of zinc foils immersed in the blank electrolyte and the 6-AA added electrolyte. Magnified XRD pattern representing (i) in the 24–36° range and (ii) in the 49–61° range.

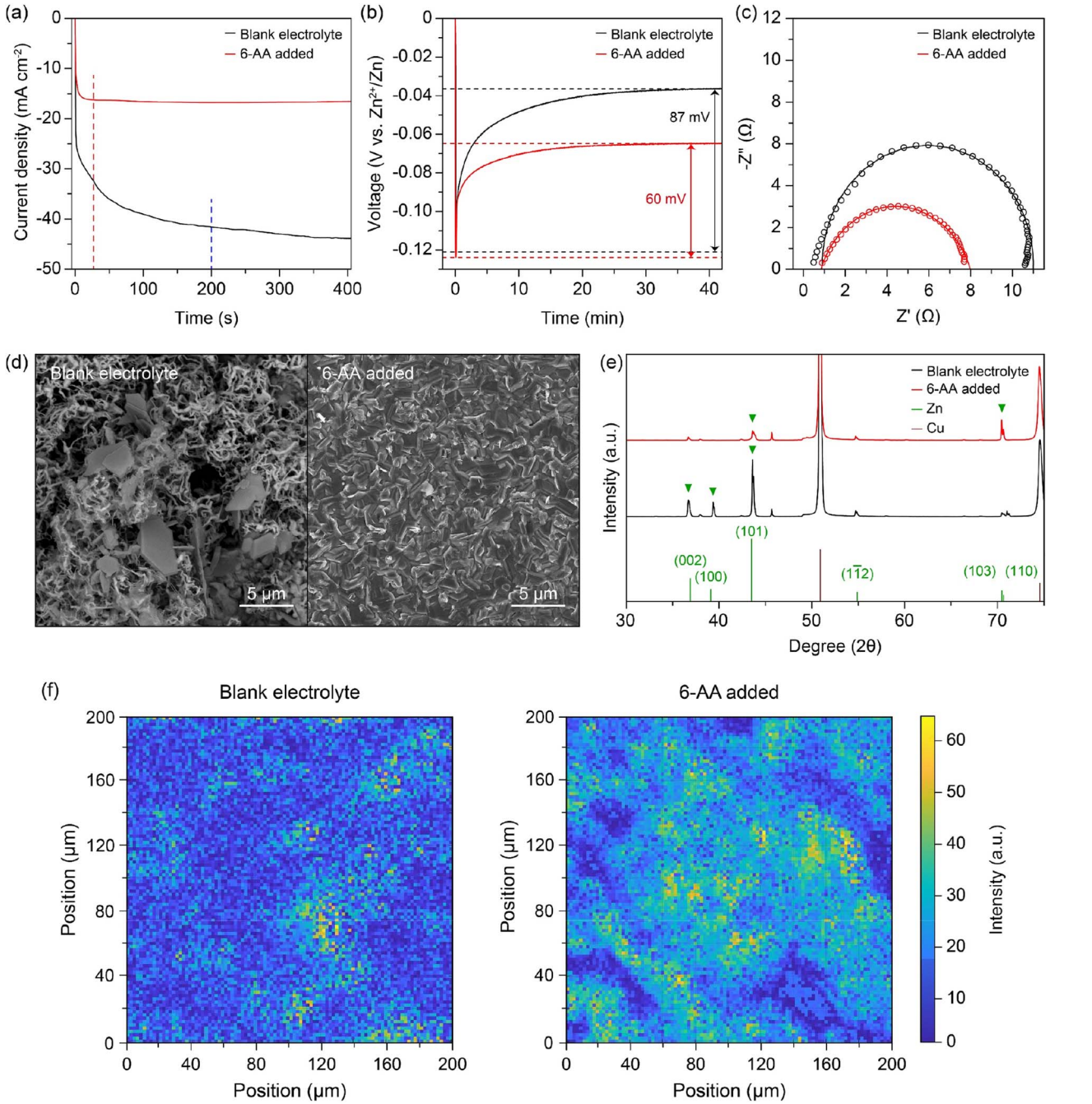

Fig. 3 (a) Chronoamperometry (CA) curves of the blank electrolyte (black) and the 6-AA added electrolyte in a zinc symmetric cell at 150 mV. (b) Zinc deposition overpotential graphs of the blank electrolyte (black) and the 6-AA added electrolyte (red) in the zinc symmetric cell at 5 mA cm^{-2}. (c) Electrochemical impedance spectroscopy (EIS) curves of the zinc symmetric cell with/without the 6-AA additive in 1 M $ZnSO_4$. (d) Top-view scanning electron microscopy (SEM) images of the Cu current collector after 29 cycles in 1 mA cm^{-2} for 1 mA h cm^{-2} with a cut-off voltage of 0.5 V *vs.* Zn^{2+}/Zn and zinc deposition at 1 mA cm^{-2} and 4 mA h cm^{-2} in the Zn||Cu cell with/without the 6-AA additive in 1 M $ZnSO_4$. (e) X-ray diffraction (XRD) patterns of the corresponding Cu current collector in Fig. 4(d). (f) X-ray fluorescence (XRF) images of the Cu current collector after 5 cycles at 1 mA cm^{-2} for 1 mA h cm^{-2} with a cut-off voltage of 0.5 V *vs.* Zn^{2+}/Zn and zinc deposition at 1 mA cm^{-2} for 1 mA h cm^{-2} in the Zn||Cu cell with/without the 6-AA additive in 1 M $ZnSO_4$. The size of XRF images is 0.2 mm × 0.2 mm.

that the adsorbed 6-AA molecules do not affect the Zn^{2+} transfer but prevent the contact of H_2O and SO_4^{2-} with the zinc metal surface. Therefore, the higher growth overpotential in the 6-AA added electrolyte results from not the high charge transfer resistance or lower Zn^{2+} binding energy, but from the smaller surface area due to homogeneous zinc deposition.

The morphology of zinc deposition on copper is determined by using a scanning electron microscope (SEM). The SEM image of the copper substrate after zinc deposition shows hexagonal deposits and string-like zinc growth on the copper surface in the blank electrolyte (Fig. 3d, left), whereas a clear surface and uniform zinc deposition are observed in the case of the 6-AA

added electrolyte (Fig. 3d, right). Moreover, the SEM images from various 6-AA concentration electrolytes show a smoother surface and fewer hexagonal deposits are formed in the 6-AA added electrolytes, especially at a concentration of 0.5 M or higher, than in the blank electrolyte (Fig. S11†). XRD analysis was conducted to confirm the uniform zinc deposition in the 6-AA added electrolyte (Fig. 3e). The XRD peaks at 36.4°, 39.1°, 43.3°, 54.5° and 70.2°, 70.7° represent the (002), (100), (101),

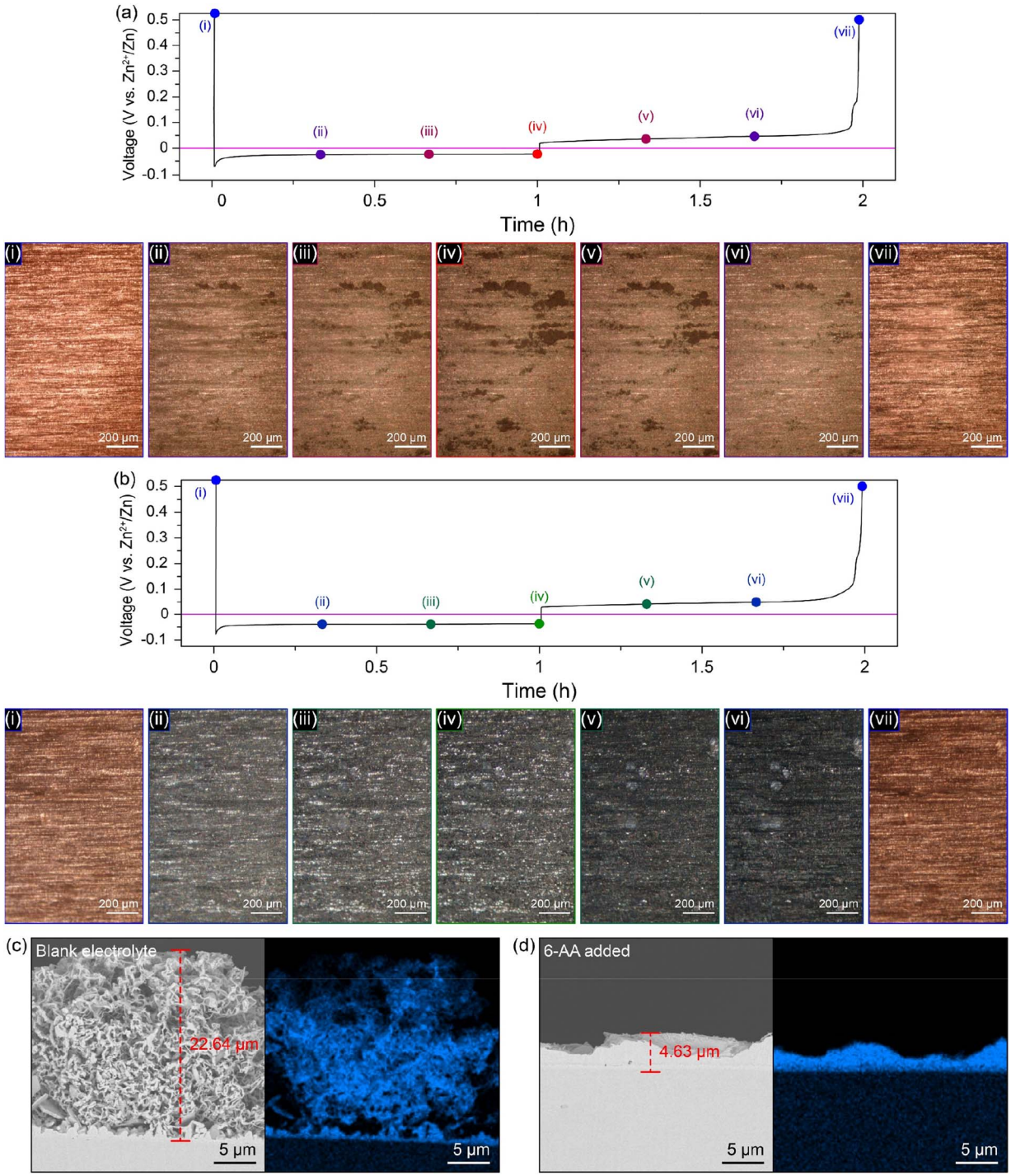

Fig. 4 Optical images obtained by top-view *operando* visualization with an optical microscope (OM) and voltage profile of the Cu current collector of the Zn||Cu cell under the deposition conditions of 1 mA cm^{-2} and 1 mA h cm^{-2} and stripping conditions of 1 mA cm^{-2} and a cut-off voltage of 0.5 V *vs.* Zn^{2+}/Zn: (a) the blank electrolyte and (b) the 6-AA added electrolyte. Optical images of (i–vii) representing (i) pristine, (ii) 0.33 mA h cm^{-2} deposited, (iii) 0.67 mA h cm^{-2} deposited, (iv) 1 mA h cm^{-2} deposited, (v) 0.33 mA h cm^{-2} stripped, (vi) 0.67 mA h cm^{-2} stripped and (vii) fully stripped with a cut-off voltage of 0.5 V *vs.* the Zn^{2+}/Zn state, respectively. (c) Cross-section scanning electron microscopy (SEM) images of the Cu current collector after 29 cycles in 1 mA cm^{-2} for 1 mA h cm^{-2} with a cut-off voltage of 0.5 V *vs.* Zn^{2+}/Zn and zinc deposition at 1 mA cm^{-2} and 4 mA h cm^{-2} (c) in the blank electrolyte and (d) in 1 M $ZnSO_4$ with the 6-AA additive.

(103), and (110) planes of hexagonal zinc crystals.[52] The XRD pattern of the blank electrolyte (black line) shows (101) oriented zinc crystal growth, which is a general zinc dendrite plane.[53,54] However, the XRD pattern of the 6-AA added electrolyte shows high intensity at the (103) plane, which is not normally observed in normal zinc deposition. According to previous research, the specific oriented zinc deposition results in non-dendritic zinc deposition, which is consistent with the CA and SEM images. Additionally, X-ray fluorescence (XRF) analysis was conducted to visualize the presence of zinc in a 0.2 mm × 0.2 mm area, which shows that the zinc metal is deposited more uniformly in the 6-AA added electrolyte than in the blank electrolyte (Fig. 3f). These results reconfirmed that the 6-AA additive ensures the uniform deposition of zinc.

For additional morphology analysis of the differences in zinc deposition on the copper substrate in different electrolytes, top-view *operando* visualization with an optical microscope (OM) was carried out (Fig. 4a, b, ESI Video 1 and 2†). The cycling conditions of the top-view Zn||Cu optical cell were a deposition current density of 1 mA cm^{-2} with a capacity of 1 mA h cm^{-2} and a stripping current density of 1 mA cm^{-2} with a cut-off voltage of 0.5 V (*vs.* Zn^{2+}/Zn). A significant growth of dark grey zinc dendrites occurs only in a specific area of the copper substrate in the blank electrolyte during the first deposition process (Fig. 4a(i–iv) and ESI Video 1†). On the other hand, a uniform growth of zinc occurs on the entire copper surface during deposition, and no further growth of zinc dendrites occurs until the end of the deposition process in the 6-AA added

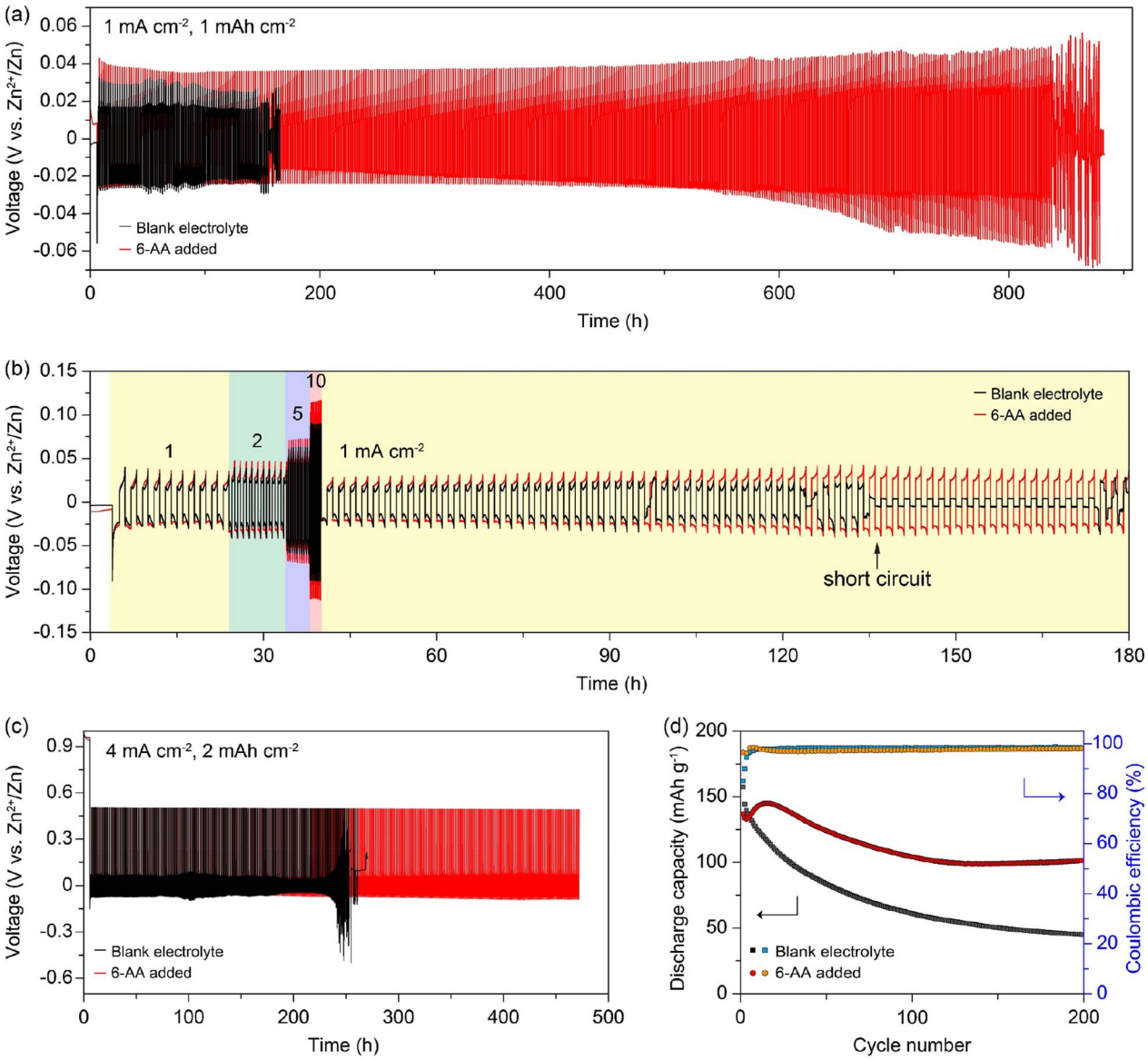

Fig. 5 (a) Voltage–time profiles of the zinc symmetric cell with/without the 6-AA additive at 1 mA cm^{-2} and 1 mA h cm^{-2}. (b) Rate properties of the zinc symmetric cell with a fixed areal capacity of 1 mA h cm^{-2} at 1, 2, 5, and 10 mA cm^{-2} for 10 cycles with the subsequent cycle conditions of 1 mA cm^{-2} and 1 mA h cm^{-2}. (c) Voltage–time profiles of the Zn||Cu cell with/without the 6-AA additive at 1 mA cm^{-2} and 1 mA h cm^{-2} and a stripping cut-off voltage of 0.5 V *vs.* Zn^{2+}/Zn. (d) Cycle performance with the Coulombic efficiency of the α-MnO_2||Zn cells, cycling at 0.5 A g^{-1} between 0.9 V and 1.8 V (*vs.* Zn^{2+}/Zn).

electrolyte (Fig. 4b(i–iv) and ESI Video 2†). Furthermore, the metallic texture surface shown in Fig. 4b(ii–iv) demonstrates that zinc metal has grown uniformly during the deposition process due to the adsorbed 6-AA molecules, which supports the XRD results shown in Fig. 3e. Also, during the stripping process, both electrolytes show reversible zinc stripping regardless of the presence of the 6-AA additive (Fig. 4a(vi–vii), b(vi–vii), ESI Video 1 and 2†). However, during the subsequent deposition process, dendritic growth is observed in the blank electrolyte optical cell, while uniform zinc deposition occurs in the 6-AA added electrolyte during the subsequent deposition process (ESI Video 1 and 2†). In addition, to observe the change of zinc deposition/stripping according to the additive concentration, top-view *operando* visualization OM was also conducted at various additive concentrations. The 0.05 M 6-AA electrolyte shows aggregated zinc deposits during the first and the subsequent deposition although the zinc deposition is more uniform than in the blank electrolyte (ESI Video 3†). In the case of 0.3 M, a slightly lower concentration than that of the standard 6-AA added electrolyte (0.5 M), more uniform deposition and a smoother metallic surface are observed compared to the blank electrolyte and 0.05 M, while the zinc clusters appear (ESI Video 4†). The higher concentration of 0.7 M electrolyte shows that the smooth surface is maintained during deposition with a reversible stripping process similar to the standard 6-AA added electrolyte (ESI Video 5†). The analysis of the surface morphology of different electrolytes revealed that the lowest concentration at which uniform zinc deposition and a metallic surface occur is 0.5 M. Cross-section SEM analysis was conducted to confirm the non-dendritic and dense zinc deposition in the 6-AA added electrolyte. The SEM image in Fig. 4c displays the growth of zinc in the blank electrolyte, demonstrating thread-like dendrites, the height of which is approximately 22.64 μm. In contrast, the SEM image of the deposited zinc in the 6-AA added electrolyte in Fig. 4d shows uniform and dense metal deposition, with a height of 4.63 μm.

To assess the effect of the 6-AA additive on the battery performance, we conducted electrochemical tests as shown in Fig. 5. Zn||Zn symmetric cells were assembled using the blank electrolyte and the 6-AA added electrolyte. Fig. 5a shows that the Zn||Zn symmetric cell with the 6-AA added electrolyte is sustained for 800 h at 1 mA cm^{-2}, while the symmetric cell with the blank electrolyte only performed for 150 h at 1 mA cm^{-2}. In addition, the rate capability of Zn||Zn symmetric cells with different electrolytes was investigated by stepwise increase from 1 to 10 mA cm^{-2} and back to 1 mA cm^{-2} for a fixed capacity of 1 mA h cm^{-2} (Fig. 5b). The cell cycled in the blank electrolyte failed due to a short circuit, while the cell in the 6-AA added electrolyte exhibited a longer cycle life than that in blank electrolyte when the current density was back to 1 mA cm^{-2}. The cycle performance of the Zn||Cu cells at higher current density was further examined (Fig. 5c). We found that the cell with the 6-AA added electrolyte delivered more than twice the cycle life than that of the blank electrolyte. The cycle performance of the 6-AA electrolyte may result from the decrease of zinc corrosion and stable zinc deposition during cycling, which reaffirms the positive effect of the 6-AA additive on the aqueous zinc metal battery. In addition, the full cell performance was evaluated by using the α-MnO_2 cathode to elucidate the possibility of practical application of the 6-AA added electrolyte (Fig. 5d). As shown in the cyclic voltammograms (CV) of the two electrolytes at 0.2 mV s^{-1} (Fig. S12†), there are no significant peak changes between the CV curves of the two electrolytes. This indicates that there is no side reaction between the 6-AA additive and α-MnO_2 during the charge/discharge process. The full cell using the 6-AA additive exhibited a higher specific capacity than that of the blank electrolyte and displayed a high Coulombic efficiency of 97.5% for 200 cycles. The corresponding voltage profiles of the two electrolytes in Fig. 5d are presented in Fig. S13,† indicating a more severe capacity drop in the blank electrolyte. Additionally, the α-MnO_2||Zn full cell at 0.2 A g^{-1} in the 6-AA added electrolyte showed better cycle performance than that of the blank electrolyte (Fig. S14†). It is suggested that the 6-AA added electrolyte can achieved better cycle performance than the blank electrolyte in real battery systems.

Conclusions

In summary, a 6-AA added electrolyte shows uniform zinc deposition and longer battery cycle. Through electrolyte analysis such as pH measurement and FTIR, it was shown that 6-AA has the property of being dissolved as a bipolar ion in the electrolyte. Additionally, side reactions such as hydrogen gas generation and zinc corrosion in the electrolyte were reduced due to the 6-AA additive, and it can be inferred that the use of an electrolyte with the 6-AA additive will inhibit the calendar aging of zinc. In the case of zinc dendrites, no significant dendrite growth was observed in the 6-AA added electrolyte, and a flat electrode surface was maintained, as observed through various electrochemical experiments and morphology analysis, while the formation of zinc dendrites was clearly observed on the surface of the electrode in the blank electrolyte. Furthermore, *operando* top-view optical visualization revealed that a metallic textured surface was formed in the 6-AA added electrolyte during the zinc deposition process, whereas a dark-grey surface and zinc dendrites were observed in the blank electrolyte. Cross-section SEM also showed dense and uniform zinc deposition in the 6-AA added electrolyte. As a result, the cycle performance in the Zn||Zn symmetric cell and Zn||Cu cell with the 6-AA added electrolyte showed improved cycle performance compared to the cells with the blank electrolyte. Additionally, the enhanced performance by the 6-AA additive was confirmed in an α-MnO_2||Zn full cell system.

Author contributions

Sung-Ho Huh: conceptualization, methodology, investigation, formal analysis, writing – original draft, and visualization. Yoon Jeong Choi: conceptualization, methodology, investigation, formal analysis, writing – original draft, and visualization. So Hee Kim: validation. Jong-Seong Bae: validation. Si-Hwan Lee: validation. Seung-Ho Yu: project administration, funding acquisition, supervision, and writing – review & editing.

Conflicts of interest

There are no conflicts to declare.

Acknowledgements

This work is supported by the National Research Foundation of Korea (NRF) grant funded by the Korea government (MSIT) (NRF-2020R1C1C1012308). J.-S. B. acknowledges the support by The Ministry of Science and ICT in Korea *via* KBSI (Grant No. C310200).

References

1 J. Y. Hwang, S. T. Myung and Y. K. Sun, *Chem. Soc. Rev.*, 2017, **46**, 3529–3614.
2 L. Cao, D. Li, T. Pollard, T. Deng, B. Zhang, C. Yang, L. Chen, J. Vatamanu, E. Hu, M. J. Hourwitz, L. Ma, M. Ding, Q. Li, S. Hou, K. Gaskell, J. T. Fourkas, X.-Q. Yang, K. Xu, O. Borodin and C. Wang, *Nat. Nanotechnol.*, 2021, **16**, 902–910.
3 N. Xu, X. Li, H. Li, Y. Wei and J. Qiao, *Sci. Bull.*, 2017, **62**, 1216–1226.
4 Z. P. Cano, D. Banham, S. Ye, A. Hintennach, J. Lu, M. Fowler and Z. Chen, *Nat. Energy*, 2018, **3**, 279–289.
5 Z. Yi, G. Chen, F. Hou, L. Wang and J. Liang, *Adv. Energy Mater.*, 2021, **11**, 2003065.
6 N. Zhang, X. Chen, M. Yu, Z. Niu, F. Cheng and J. Chen, *Chem. Soc. Rev.*, 2020, **49**, 4203.
7 Z. Zhou, Y. Zhang, P. Chen, Y. Wu, H. Yang, H. Ding, Y. Zhang, Z. Wang, X. Du and N. Liu, *Chem. Eng. Sci.*, 2019, **194**, 142–147.
8 Q. Zhang, J. Luan, L. Fu, S. Wu, Y. Tang, X. Ji and H. Wang, *Angew. Chem., Int. Ed.*, 2019, **58**, 15841–15847.
9 M. Yan, P. He, Y. Chen, S. Wang, Q. Wei, K. Zhao, X. Xu, Q. An, Y. Shuang, Y. Shao, K. T. Mueller, L. Mai, J. Liu and J. Yang, *Adv. Mater.*, 2018, **30**, 1703725.
10 M. He, C. Shu, A. Hu, R. Zheng, M. Li, Z. Ran and J. Long, *Energy Storage Mater.*, 2022, **44**, 452–460.
11 X. Liu, F. Yang, W. Xu, Y. Zeng, J. He and X. Lu, *Adv. Sci.*, 2020, **7**, 2002173.
12 Z. Zhao, J. Zhao, Z. Hu, J. Li, J. Li, Y. Zhang, C. Wang and G. Cui, *Energy Environ. Sci.*, 2019, **12**, 1938–1949.
13 B. Li, X. Zhang, T. Wang, Z. He, B. Lu, S. Liang and J. Zhou, *Nano-Micro Lett.*, 2022, **14**, 6.
14 M. Kwon, J. Lee, S. Ko, G. Lim, S.-H. Yu, J. Hong and M. Lee, *Energy Environ. Sci.*, 2022, **15**, 2889–2899.
15 L. Wang, W. Huang, W. Guo, Z. H. Guo, C. Chang, L. Gao and X. Pu, *Adv. Funct. Mater.*, 2022, **32**, 2108533.
16 S.-B. Wang, Q. Ran, R.-Q. Yao, H. Shi, Z. Wen, M. Zhao, X.-Y. Lang and Q. Jiang, *Nat. Commun.*, 2020, **11**, 1–9.
17 H. Tao, Z. Hou, L. Zhang, X. Yang and L.-Z. Fan, *Chem. Eng. J.*, 2022, **450**, 138048.
18 X. Guo, Z. Zhang, J. Li, N. Luo, G.-L. Chai, T. S. Miller, F. Lai, P. Shearing, D. J. L. Brett, D. Han, Z. Weng, G. He and I. P. Parkin, *ACS Energy Lett.*, 2021, **6**, 395–403.
19 Z. Wu, M. Li, Y. Tian, H. Chen, S.-L. Zhang, C. Sun, C. Li, M. Kiefel, C. Lai, Z. Lin and S. Zhang, *Nano-Micro Lett.*, 2022, **14**, 110.
20 X. Zeng, K. Xie, S. Liu, S. Zhang, J. Hao, J. Liu, W. K. Pang, J. Liu, P. Rao, Q. Wang, J. Mao and Z. Guo, *Energy Environ. Sci.*, 2021, **14**, 5947–5957.
21 Z. Jia, W. Zhao, S. Hu, X. Yang, T. He and X. Sun, *Chem. Commun.*, 2022, **58**, 8504–8507.
22 H. Qin, W. Kuang, N. Hu, X. Zhong, D. Huang, F. Shen, Z. Wei, Y. Huang, J. Xu and H. He, *Adv. Funct. Mater.*, 2022, **32**, 2206695.
23 C. Huang, X. Zhao, Y. Yang, Y. Qian, G. Chang, Y. Zhang, Q. Tang, A. Hu and X. Chen, *Small*, 2022, **18**, 2203674.
24 L. D. Ellis, J. P. Allen, L. M. Thompson, J. E. Harlow, W. J. Stone, I. G. Hill and J. R. M. Dahn, *J. Electrochem. Soc.*, 2017, **164**, A3518–A3528.
25 J. Seok, J.-H. Hyun, A. Jin, J. H. Um, H. D. Abruña and S.-H. Yu, *ACS Appl. Mater. Interfaces*, 2022, **14**, 10438–10446.
26 J. Seok, C. N. Gannett, S.-H. Yu and H. D. Abruña, *Anal. Chem.*, 2021, **93**, 15459–15467.
27 H. Dong, X. Hu and G. He, *Nanoscale*, 2022, **14**, 14544–14551.
28 S. A. Rahmani, A. Meidianto, M. I. Amal, A. S. Wismogroho and W. B. Widayatno, *J. Phys.: Conf. Ser.*, 2018, **985**, 012033.
29 J. Joseph and E. D. Jemmis, *J. Am. Chem. Soc.*, 2007, **129**, 4620–4632.
30 X. Chang, Y. Zhang, X. Weng, P. Su, W. Wu and Y. Mo, *J. Phys. Chem. A*, 2016, **120**, 2749–2756.
31 C. Branca, G. D'Angelo, C. Crupi, K. Khouzami, S. Rifici, G. Ruello and U. Wanderlingh, *Polymer*, 2016, **99**, 614–622.
32 D. Stefanakis, A. Philippidis, L. Sygellou, G. Filippidis, D. Ghanotakis and D. Anglos, *J. Nanopart. Res.*, 2014, **16**, 2646.
33 J. D. Patel, F. Mighri, A. Ajji and S. Elkoun, *Mater. Sci. Appl.*, 2012, **3**, 125–130.
34 M. Windholz, *The Merck Index: and Encyclopedia of Chemicals, Drugs, and Biologicals*, Merck & Co., Rahway, New Jersey, 1983.
35 M. A. Raza, P. D. Hallett, X. Liu, M. He and W. Afzal, *J. Chem. Eng. Data*, 2019, **64**, 5049–5056.
36 J. Arts, S. Bade, M. Badrinas, N. Ball and S. Hindle, *Regul. Toxicol. Pharmacol.*, 2018, **97**, 197–208.
37 A. V. Marukhlenko, M. A. Morozova, A. M. J. Mbarga, N. V. Antipova, A. V. Syroeshkin, I. V. Podoprigora and T. V. Maksimova, *Pharmaceuticals*, 2022, **15**, 979.
38 Y. Li, S. Yang, H. Du, Y. Liu, X. Wu, C. Yin, D. Wang, X. Wu, Z. He and X. Wu, *J. Mater. Chem. A*, 2022, **10**, 14399–14410.
39 P. Wang, S. Liang, C. Chen, X. Xie, J. Chen, Z. Liu, Y. Tang, B. Lu and J. Zhou, *Adv. Mater.*, 2022, **34**, 2202733.
40 W. W. Rudolph, M. H. Brooker and P. Tremaine, *Z. Phys. Chem.*, 1999, **209**, 181–207.
41 J. Xu, W. Lv, W. Yang, Y. Jin, Q. Jin, B. Sun, Z. Zhang, T. Wang, L. Zheng, X. Shi, B. Sun and G. Wang, *ACS Nano*, 2022, **16**, 11392–11404.
42 N. Ghosh, S. Roy, A. Bandyopadhyay and J. A. Mondal, *Liquids*, 2023, **3**, 19–39.
43 K. Wu, J. Cui, J. Yi, X. Liu, F. Ning, Y. Liu and J. Zhang, *ACS Appl. Mater. Interfaces*, 2022, **14**, 34612–34619.
44 C. Huang, X. Zhao, Y. Hao, Y. Yang, Y. Quan, G. Chang, Y. Zhang, Q. Tang, A. Hu, Z. Liu and X. Chen, *J. Mater. Chem. A*, 2022, **10**, 6636–6640.

45 X. Shan, S. Kim, A. M. M. Abeykoon, G. Kwon, D. Olds and X. Teng, *ACS Appl. Mater. Interfaces*, 2020, **12**, 54627–54636.
46 A. Šarić, M. Vrankić, D. Lützenkirchen-Hecht, I. Despotović, Ž. Petrović, G. Dražić and F. Eckelt, *Inorg. Chem.*, 2022, **61**, 2962–2979.
47 C. Fu, Y. Wang, C. Lu, S. Zhou, Q. He, Y. Hu, M. Feng, Y. Wan, J. Lin, Y. Zhang and A. Pan, *Energy Storage Mater.*, 2022, **51**, 588–598.
48 L. Miao, R. Wang, S. Di, Z. Qian, L. Zhang, W. Xin, M. Liu, Z. Zhu, S. Chu, Y. Du and N. Zhang, *ACS Nano*, 2022, **16**, 9667–9678.
49 Q. Zhang, J. Luan, Y. Tang, X. Ji and H. Wang, *Angew. Chem., Int. Ed.*, 2020, **59**, 13180–13191.
50 A. Pen, G. Zheng, F. Shi, Y. Li and Y. Cui, *Nano Lett.*, 2017, **17**, 1132–1139.
51 K. N. Wood, E. Kazyak, A. F. Chadwick, K.-H. Chen, J.-G. Zhang, K. Thornton and N. P. Dasgupta, *ACS Cent. Sci.*, 2016, **2**, 790–801.
52 J. Nuss, U. Wedig, A. Kirfel and M. Jansen, *Z. Anorg. Allg. Chem.*, 2010, **636**, 309–313.
53 M. Zhou, S. Guo, J. Li, X. Luo, Z. Liu, T. Zhang, X. Cao, M. Long, B. Lu, A. Pan, G. Fang, J. Zhou and S. Liang, *Adv. Mater.*, 2021, **33**, 2100187.
54 J. Zheng, J. Yin, D. Zhang, G. Li, D. C. Bock, T. Tang, Q. Zhao, X. Liu, A. Warren, Y. Deng, S. Jin, A. C. Marschilok, E. S. Takeuchi, K. J. Takeuchi, C. D. Rahn and L. A. Archer, *Sci. Adv.*, 2020, **6**, eabb1122.